

Global Accretion Properties of Black Hole X-Ray Binaries: A Phenomenological Perspective

Arghajit Jana^{1*},

¹*Institute of Astronomy, National Tsing Hua University, Hsinchu, 30013, Taiwan*

Accepted XXX. Received YYY; in original form ZZZ

ABSTRACT

Black hole X-ray binaries (BHXBs) show rich phenomenology in the spectral and timing properties. We collected the spectral data of 20 BHXBs from the literature across different spectral states. The spectral properties are studied in the forms of the inner disc temperature (T_{in}), photon index (Γ), hot electron temperature (kT_e), X-ray flux (F_X) and luminosity (L_X). We studied various correlations among different spectral parameters to understand the accretion process on a global scale. In the thermal soft states (TSS), we find most of the sources followed $F_{\text{disc}} \propto T_{\text{in}}^4$ relation. A ‘V’-shaped correlation is found between Γ and total luminosity (L_{tot}) in the hard Comptonized state (HCS). The Comptonized luminosity is observed to be correlated with the disc luminosity in the HCS and TSS. No notable correlation is observed in the intermediate state (IMS). The evolution of the inner disc radius (R_{in}) is unclear in the HCS and IMS. We also discuss how the hot electron temperature changes with other spectral parameters. We observe that the iron line flux correlates with disc and Comptonized fluxes. The strength of the reprocessed emission is found to vary across spectral states.

Key words: X-Rays:binaries – stars:black holes – accretion, accretion discs

1 INTRODUCTION

A transient black hole X-ray binary (BHXB) spends most of the time in a quiescent state with very low X-ray luminosity ($L_X < 10^{32}$ erg s⁻¹) and occasionally goes to outburst that lasts from several weeks to months (e.g., Remillard & McClintock 2006; Tetarenko et al. 2016). The X-ray luminosity increases a few orders of magnitude during the outburst compared to the quiescent state. On the other hand, a persistent source is found to be always active with the X-ray luminosity $L_X > 10^{35}$ erg s⁻¹.

An X-ray spectrum of BHXBs can be approximated by a multi-colour blackbody (MCD) component and a power-law tail (PL). The geometrically thin and optically thick accretion disc is believed to be the origin of the MCD (Shakura & Sunyaev 1973), while the hard PL tail originates in a Compton corona, located close to the BH (e.g., Haardt & Maraschi 1993; Chakrabarti & Titarchuk 1995; Done et al. 2007). A fraction of the seed photons up-scatter with the hot electrons of the Compton corona and produce a power-law tail via inverse-Comptonization (Sunyaev & Titarchuk 1980, 1985). Further, a fraction of the hard photons is reprocessed in the disc and produces an iron

$K\alpha$ line at ~ 6.4 keV and a reflection hump at ~ 20 –40 keV (e.g., Fabian et al. 1989; Matt et al. 1991).

The BHXBs also exhibit low-frequency quasi-periodic oscillations (LFQPOs) in the power-density spectra (PDS) observed in a range of 0.1 – 20 Hz (see, Remillard & McClintock 2006; Ingram & Motta 2019, for a review). Depending on the the Q-factor ($Q = \nu/\Delta\nu$, ν and $\Delta\nu$ are centroid frequency and full width at half-maximum; FWHM), the rms amplitude, a LFQPO can be classified as Type-A, Type-B, or Type-C (Casella et al. 2005, and references therein).

During the outburst phase, a BHXB shows fast variability and fluctuation in the spectral and timing properties (e.g., Van der Klis 1989, 1994; Méndez & van der Klis 1997). A correlation between the spectral and timing properties is seen in the hardness–intensity diagram (HID; e.g., Homan et al. 2001; Homan & Belloni 2005), accretion rate–intensity diagram (ARRID; e.g., Mondal et al. 2014; Jana et al. 2016), rms–intensity diagram (RID; e.g., Muñoz-Darias et al. 2011) or hardness–rms diagram (HRD; e.g., Belloni et al. 2005). Commonly, two major spectral states are observed in BHXBs: hard Comptonized state (HCS) and thermal soft state (TSS; e.g., Belloni et al. 2005; Remillard & McClintock 2006; Nandi et al. 2012). In between HCS and TSS, an intermediate state (IMS) is also ob-

* E-mail: janaarghajit@mx.nthu.edu.tw, argha0004@gmail.com

served (e.g., [Remillard & McClintock 2006](#)). A BHXB transits from the HCS to TSS or vice-versa through the IMS, i.e., IMS acts as the state transition phase. Sometimes, the IMS is further divided into hard intermediate state (HIMS) and soft-intermediate state (SIMS). An outbursting BHXB is generally found to evolve as $\text{HCS} \rightarrow \text{HIMS} \rightarrow \text{SIMS} \rightarrow \text{TSS} \rightarrow \text{SIMS} \rightarrow \text{HIMS} \rightarrow \text{HCS}$. A BHXB goes through all the spectral states in a complete outburst. However, some outbursts do not show TSS and are known as the ‘failed’ outburst (e.g., [Tetarenko et al. 2016](#); [Debnath et al. 2017](#)).

A BHXB shows rich phenomenology across all the spectral states. Each spectral state is characterized by different spectral and timing properties (e.g., [Remillard & McClintock 2006](#); [Done et al. 2007](#)). A HCS spectrum is characterized by a cool disc of temperature $T_{\text{in}} \sim 0.1 - 0.5$ keV, and photon index, $\Gamma \sim 1.5 - 1.7$. The disc component is not observed sometimes in the HCS. The hard X-ray photon flux dominates over the soft photon flux in this state. BHXBs also exhibit a compact and quasi-stable jet in the HCS (e.g., [Fender & Belloni 2004](#)). In this state, an evolving type-C QPO is observed. The TSS spectra can be described by a disc of a temperature, $T_{\text{in}} \sim 1$ keV and photon index, $\Gamma > 2.3$. No jet is observed in this state. QPOs also are not observed in the TSS. The source transit to the TSS from the HCS via an IMS, i.e. HIMS and SIMS. In these spectral states, the soft and hard photon fluxes are comparable. The IMS is often seen to be associated with the discrete ejection or blobby jet (e.g., [Nandi et al. 2001](#); [Fender & Belloni 2004](#)). Evolving type-C QPOs are generally observed in the HIMS, while sporadic type-A or type-B QPOs are observed in the SIMS.

The phenomenology of the BHXBs can be studied in terms of the disc temperature (T_{in}), photon index (Γ) and X-ray flux (F_{X}). Correlations among different spectral parameters and the evolution of the timing and spectral parameters are well established. Here, we revisited the phenomenological properties and different correlations among them to test if these relations hold globally. Here, we gathered information on the spectral parameters for 20 BHXBs across different spectral states. We studied various correlations among the sources individually and with the entire sample across all the spectral states. The paper is organized in the following way: In §2, we described the sample. Then, the analysis process and results are presented in §3. Finally, in §4, we discussed our findings.

2 SAMPLE SELECTION AND DATA ACQUISITION

2.1 Sample

We selected the sources from the literature where the outburst evolution of the sources is studied. We chose the sources where the information of inner disc temperature (T_{in}), disc normalization (N_{DBB}) or inner disc radius (R_{in}), photon index (Γ), disc flux (F_{disc}), Comptonized flux (F_{Compt}) and line flux (F_{line}) are available. In total, we selected 32 outbursts of 20 sources for our study. Out of a total of 20 sources, we selected one outburst each for 16 sources, two outbursts each for two sources, and six outbursts for two sources. GX 339–4 and H 1743–322 showed $\sim 8 - 10$ outbursts in the last 25 years. However, we chose only six

outbursts for each source where the information on spectral evolution was available. We did not include the data of any persistent sources in this work. The information about the outburst is tabulated in Table 1.

2.2 Mass, Distance and Inclination

We collected the information on the mass (M_{BH}), distance (d) and inclination angle (i) of the sources from the literature. The information of the mass, distance and inclination angle are available from 15, 15 and 13 sources, respectively. When no information is available, we assumed $M_{\text{BH}} = 8 M_{\odot}$, $d = 5$ kpc and $i = 45$ degrees in our study. The details information is presented in Table 1.

2.3 Spectral Parameters

In the present study, we concentrated on the spectral properties of BHXBs. In this work, we studied the disc, Comptonized and iron line emission of BHXBs. As most of the studies were done using RXTE/PCA data up to 20 keV, the study of the reflection was scarce. However, iron $K\alpha$ line, which is produced via reflection, is detected at ~ 6.4 keV. The spectra were analysed using a multi-colour disc blackbody (MCD), a Comptonized component and iron line emission. The MCD emission was modelled with the XSPEC model DISKBB ([Mitsuda et al. 1984](#); [Makishima et al. 1986](#)) and the Comptonized emission was modelled with the XSPEC model POWER-LAW (PL), CUTOFF POWER-LAW (CPL) or COMPTT model ([Titarchuk 1994](#)). The iron line emission was modelled with a Gaussian component at ~ 6.4 keV.

From these spectral modelling, we acquired the information of inner disc temperature (T_{in}), photon index (Γ), cut-off energy (E_{cut}), disc flux (F_{disc}), Comptonized flux (F_{Compt}) and line flux (F_{line}). From the DISKBB normalization (N_{dabb}), we obtained the inner disc radius (R_{in}). The N_{dabb} is given by, $N_{\text{dabb}} = (r_{\text{in}}/d_{10})^2 \cos i$, where r_{in} , d_{10} and i are the apparent inner disc radius, distance in 10 kpc and disc inclination angle. The apparent radius (r_{in}) is related to the true inner disc radius (R_{in}) as $R_{\text{in}} = \xi \kappa^2 r_{\text{in}}$, where ξ and κ are correction factor and spectral colour correction factor, respectively (e.g., [Shimura & Takahara 1995](#); [Kubota et al. 1998](#)). We used $\xi = 0.41$ ([Kubota et al. 1998](#)) and $\kappa = 1.8$ for our calculation.

The E_{cut} is related to the kT_e as $E_{\text{cut}} \sim 2 - 3 kT_e$ (e.g., [Petrucci et al. 2001](#)). In our analysis, we collected the information of kT_e and E_{cut} in the HCS from the literature. We used $E_{\text{cut}} = 2kT_e$ in our analysis, which is a reasonable approximation. The reflection fraction often measures the strength of the reflection (R_{ref}), which is defined as the ratio of the reflected emission to the direct emission to the observer. In this study, we used the ratio of the iron line flux to the Comptonized flux ($F_{\text{line}}/F_{\text{Compt}}$) as a proxy of the reflection fraction.

2.4 Luminosity and Bolometric Correction

We collected the information on the disc flux (F_{disc}) and Comptonized flux (F_{Compt}) from the literature. In most cases, the fluxes were reported in a narrow energy band

Table 1. List of Sources

No	Name	Mass (M_{\odot})	Dist (kpc)	Incl. (deg)	Outburst	Telescope	Energy Range (keV)	Ref.
1	GRS 1716–249	5.0 ± 0.7	2.4 ± 0.4	40 – 50	2017	Swift/XRT Swift/BAT	0.5 – 10 15 – 185	1,2,3, 4
2	GX 339–4	9.0 ± 1.5	8.4 ± 0.9	30 ± 1	1996–1999, 2002, 2004	RXTE/PCA	2 – 25	5, 6, 7, 8, 9
3	H 1743–322	11.2 ± 1.9	8.5 ± 0.8	75 ± 3	2003, 2008, 2009, 2010a, 2010b, 2011	RXTE/HEXTE RXTE/PCA	18 – 200 2 – 25	10, 11, 12, 13, 14, 15, 16
4	MAXI J0637–430	8.5 ± 3.5	8.0	64 ± 6	2019–20	NICER	0.7 – 10	17, 18
5	MAXI J1348–630	9.1 ± 1.6	2.2 ± 0.6	29.2 ± 0.5	2019	Swift/XRT Swift/BAT	0.5 – 10 15 – 150	19, 20, 21
6	MAXI J1535–571	8.9 ± 1.0	4.1 ± 0.5	57 ± 2	2017	Swift/XRT	0.5 – 10	22, 23, 24, 25
7	MAXI J1659–152	6.0 ± 1.5	8.6 ± 3.7	70 – 80	2010	RXTE/PCA	2 – 25	26, 27, 28, 29
8	MAXI J1727–203	10 ± 2	5*	45*	2018	NICER	0.5 – 10	30
9	MAXI J1813–095	7.4 ± 1.5	6.0	28 – 45	2018	NICER Swift/XRT	0.5 – 10 0.5 – 10	31, 32
10	MAXI J1836+194	9.5 ± 1.5	7.0 ± 3.0	4 – 15	2011	RXTE/PCA	2 – 25	33, 34, 35
11	Swift J1357.2–0933	5.4 ± 1.4	1.5	70	2011	Swift/XRT	0.5 – 10	36, 37, 38, 39
12	Swift J1753.2–0127	5.3 ± 0.6	4 – 8	40 – 55	2005	Swift/XRT RXTE/PCA	0.5 – 10 2 – 25	40, 41, 42, 43
13	Swift J1842.5+1124	8*	5*	45*	2008	Swift/XRT RXTE/PCA	0.5 – 10 3 – 25	44
14	XTE J1118+480	7.0 ± 0.7	1.8	68 – 79	2000, 2005	RXTE/PCA	3 – 25	45, 46, 47, 48
15	XTE J1550–564	10.4 ± 2.3	4.4 ± 0.5	57 – 77	1998, 2000	RXTE/PCA RXTE/HEXTE	2 – 20 20 – 200	49, 50, 51, 52, 53
16	XTE J1652–453	8*	5*	45*	2009	Swift/XRT RXTE/PCA	0.5 – 10 2 – 25	54
17	XTE J1748–288	8*	5*	45*	1998	RXTE/PCA	3 – 25	55
18	XTE J1817–330	8*	5*	45*	2006	RXTE/PCA	2 – 25	56, 57
19	XTE J1908+094	6.5 ± 0.7	10 ± 1	27 ± 3	2002–03	RXTE/PCA	2 – 25	59, 60, 61, 62
20	XTE J2012+381	8*	5*	45*	1998	RXTE/PCA	3 – 20	63

* Estimation not available, values assumed in this work.

Errors are quoted when available.

(1) Chatterjee et al. (2021b), (2) Della Valle et al. (1994), (3) Tao et al. (2019), (4) Bassi et al. (2019), (5) Sreehari et al. (2019), (6) Parker et al. (2007), (7) Dinçer et al. (2012), (8) Nandi et al. (2012), (9) Shui et al. (2021), (10) Molla et al. (2017), (11) Steiner et al. (2012), (12) McClintock et al. (2006), (13) Kalemci et al. (2006), (14) Capitanio et al. (2009), (15) Chen et al. (2010), (16) Zhou et al. (2013), (17) Jana et al. (2021a), (18) Lazar et al. (2020), (19) Jana et al. (2020), (20) Chauhan et al. (2021), (21) Jia et al. (2022), (22) Shang et al. (2019), (23) Chauhan et al. (2019), (24) Xu et al. (2018), (25) Tao et al. (2018), (26) Stiele & Kong (2018), (27) Molla et al. (2016), (28) Kuulkers et al. (2013), (29) Torres et al. (2021), (30) Debnath et al. (2020), (31) Alabarta et al. (2020), (32) Jana et al. (2021b), (33) Armas Padilla et al. (2019), (34) Jana et al. (2016), (35) Russell et al. (2014a), (36) Mondal & Chakrabarti (2019), (37) Armas Padilla et al. (2014), (38) Stiele & Kong (2018), (39) Armas Padilla et al. (2013), (40) Debnath et al. (2019), (41) Cadolle Bel et al. (2007), (42) Neustroev et al. (2014), (43) Shaw et al. (2016), (44) Zhao et al. (2016), (45) Chatterjee et al. (2019), (46) McClintock et al. (2006), (47) Khargharia et al. (2013), (48) Debnath et al. (2020), (49) Orosz et al. (2002), (50) Orosz et al. (2011), (51) Kreidberg et al. (2012), (52) Sobczak et al. (2019), (53) Rodriguez et al. (2003), (54) Han et al. (2011), (55) Revnivtsev et al. (2000), (56) Rykoff et al. (2007), (57) Gierliński et al. (2008), (58) Chatterjee et al. (2019), (59) Curran et al. (2015), (60) Draghis et al. (2021), (61) Göğüş et al. (2004), (62) Vasiliev et al. (2000).

of 0.5 – 20 keV or similar. One needs to study the spectra in a broad energy range to gain insightful information. Hence, we calculated the bolometric flux in the energy range of 0.1 – 500 keV by applying a bolometric correction to the fluxes obtained in a limited energy band. Maccarone (2003) applied bolometric correction assuming the spectra in the form of $\frac{dN}{dE} \sim E^{-1.8} \exp^{-E/200 \text{ keV}}$ in the energy range of 0.5 keV – 10 MeV. They noted that if Γ is changed by 0.1, the flux will change by 10%, which is less than other uncertainties. Vahdat Motlagh et al. (2019) calculated disc flux in the range of 0.01 – 200 keV and power-law flux in the range of T_{in} to 200 keV. Dunn et al. (2010) calculated the disc flux in the energy range of 0.001 – 100 keV and power-law flux in the 1 – 100 keV.

Here, we calculated the disc flux in the 0.001 – 10 keV

and Comptonized power-law flux in the range between T_{in} to 500 keV, when the disc was detected. When the disc was not detected, we calculated the Comptonized flux in the energy range of 0.1 – 500 keV. As the disc is unlikely to contribute significantly over $\sim 5 - 6$ keV, we only calculated the disc luminosity up to 10 keV. To calculate the Comptonized flux, we applied bolometric correction assuming the spectra in the form of $\frac{dN}{dE} \sim E^{-\Gamma} \exp^{-E/200 \text{ keV}}$. Once we calculated the bolometric disc and Comptonized flux, we calculated the luminosity using, $L = 4\pi d^2 F$, where d is the source distance. The total luminosity is calculated as $L_{\text{tot}} = L_{\text{disc}}^{0.001-10 \text{ keV}} + L_{\text{Compt}}^{0.1-500 \text{ keV}}$. The hardness ratio (HR), disc fraction (f_{disc}) and Comptonized fraction (f_{Compt}) were calculated as $\text{HR} = L_{\text{Compt}}/L_{\text{disc}}$, $f_{\text{disc}} = L_{\text{disc}}/L_{\text{tot}}$, $f_{\text{Compt}} = L_{\text{Compt}}/L_{\text{tot}}$, respectively.

We calculated Eddington scaled luminosity or Eddington ratio (λ_{Edd}) by taking the ratio of the luminosity to the Eddington luminosity (L_{Edd}), i.e. $\lambda_{\text{Edd}} = L/L_{\text{Edd}}$. The Eddington ratio is given by $L_{\text{Edd}} = 1.3 \times 10^{38} (M_{\text{BH}}/M_{\odot})$. We calculated total Eddington ratio (λ_{tot}), disc Eddington ratio (λ_{disc}) and Comptonized Eddington ratio (λ_{Compt}) as $\lambda_{\text{tot}} = L_{\text{tot}}/L_{\text{Edd}}$, $\lambda_{\text{disc}} = L_{\text{disc}}/L_{\text{Edd}}$ and $\lambda_{\text{Compt}} = L_{\text{Compt}}/L_{\text{Edd}}$, respectively.

3 ANALYSIS AND RESULT

3.1 Flux and Luminosity

The standard thin disc emits thermal soft photons. A fraction of the thermal photons intercept in the Compton corona, and in turn, the Compton corona produces the Comptonized power-law spectra via inverse-Comptonization. Thus, in a way, the Comptonized emission is related to the thermal emission. The left panel of Figure 1 shows the variation of the F_{Compt} as a function of the F_{disc} . In the right panel of Figure 1, we plot the L_{Compt} as a function of the L_{disc} . The magenta, green and orange points represent the data from the HCS, IMS and TSS, respectively. In the right panel of Figure 1, the blue, dark green and red solid lines represent the linear best fit in the HCS, IMS and TSS, respectively. We excluded the sources with unknown distances in the right panel of Figure 1. In our sample, out of 32 outbursts, the HCS, IMS and TSS were observed in 31, 20 and 14 outbursts, respectively. In many observations in the HCS, the disc was not detected. Those observations were excluded in Figure 1.

We found that the F_{disc} and F_{Compt} are moderately correlated in all the spectral states, with the Pearson correlation coefficient $r = 0.671$ with the p-value of $< 10^{-4}$ in the HCS, $r = 0.541$ with the p-value of $< 10^{-4}$ in the IMS, and $r = 0.457$ with the p-value of $< 10^{-4}$ in the TSS, respectively. In terms of luminosity, we observed a strong correlation between L_{disc} and L_{Compt} in the HCS and a moderate correlation in the TSS. The Pearson correlation coefficient between L_{disc} and L_{Compt} was observed to be $r = 0.805$ with the p-value of $< 10^{-4}$ and $r = 0.556$ with the p-value of $< 10^{-4}$ in the HCS and TSS, respectively. Surprisingly, no correlation was observed in the IMS.

We also conducted a similar study using the Eddington ratio (λ), replacing the luminosity and obtained a similar result. We found that λ_{disc} and λ_{Compt} are strongly correlated in the HCS with the Pearson correlation coefficient as $r = 0.794$ with the p-value of $< 10^{-4}$. In the TSS, a moderate correlation was found with the Pearson correlation coefficient of $r = 0.589$ with the p-value of $< 10^{-4}$. As before, no correlation was observed in the IMS.

3.2 Photon Index

The HCS data were available for 31 outbursts from 19 sources in our sample. The thermal disc emission was not detected in $\sim 60\%$ observations within the sample. When the disc was detected, the disc fraction ($L_{\text{disc}}/L_{\text{tot}}$) was always $< 25\%$. We found that the Γ is anti-correlated with the L_{Compt} and the L_{tot} with the Pearson correlation coefficient $r = -0.599$ with the p-value of $< 10^{-4}$ and $r = -0.608$ with

the p-value of $< 10^{-4}$, respectively, in the HCS. We did not observe any correlations of the Γ with L_{Compt} and L_{tot} in the TSS and IMS. We also checked if the Γ is correlated with the HR or Comptonized fraction (f_{Compt}) across the spectral states. We did not find any correlation/anti-correlation between Γ and HR or f_{Compt} in any spectral states. A similar result was found while studying the correlation of Γ with λ_{Compt} and λ_{tot} .

The left panel of Figure 2 shows the variation of the Γ as a function of the L_{tot} in our sample. We did not include the sources with unknown distances in the plot. The blue dashed line represents the linear fit of the data. From the linear regression, we obtained $\Gamma = -(0.12 \pm 0.006)L_{\text{tot}} + (6.05 \pm 0.24)$. The Pearson correlation coefficient between Γ and L_{tot} was found to be $r = 0.518$ with the p-value of $< 10^{-4}$. This indicated a moderate negative correlation between these two parameters. We noticed that the anti-correlation weakens at the higher luminosity, indicating a ‘V’-shaped correlation. Thus, we fitted the data in two regions of luminosity. We used the following linear relation for regression analysis,

$$\begin{aligned} Y(X) &= A_1(X - X_t) + B_1 \quad (X < X_t) \\ &= A_2(X - X_t) + B_2 \quad (X > X_t). \end{aligned} \quad (1)$$

Here, replacing $Y(X)$, X and X_t with Γ , $\log L_{\text{tot}}$ and $\log(L_t)$, we obtained a negative correlation for the low-luminosity region ($L_{\text{tot}} < L_t$) and a positive correlation for the high luminosity region ($L_{\text{tot}} > L_t$). The slope was found to flip at $\log L_t \approx 37.2$, i.e. at $L_t \approx 1.5 \times 10^{37} \text{ erg s}^{-1}$. We obtained the slope of the fits as $A_1 = -0.16 \pm 0.02$ for $L \lesssim 10^{37.2}$ and $A_2 = 0.03 \pm 0.01$ for $L_{\text{tot}} \gtrsim 10^{37.2}$. In the left panel of Figure 2, the vertical line represents the transition luminosity (L_t). The dark green and black lines represent the best-fit line for $L_{\text{tot}} < L_t$ and $L_{\text{tot}} > L_t$, respectively.

The right panel of Figure 2 shows the variation of the Γ as a function of the λ_{tot} . We did not include sources with unknown masses and distances in this plot. Using linear regression analysis, we obtained a negative correlation between the Γ and λ_{tot} . The linear regression analysis returned as $\Gamma = (-0.12 \pm 0.006)\lambda_{\text{tot}} + (1.35 \pm 0.10)$. We obtained the Pearson correlation coefficient as $r = -0.608$ with the p-value $< 10^{-4}$. Similar to $\Gamma - L_{\text{tot}}$ relation, the correlation of $\Gamma - \lambda_{\text{tot}}$ is also observed to flip. Replacing $Y(X)$, X and X_t with Γ , $\log \lambda_{\text{tot}}$ and λ_t in Equation 1, we observed that the turnover happens at $\log \lambda_t \approx -2$. We obtained the slope as $A_1 = 0.19 \pm 0.02$ for $\lambda_{\text{tot}} < \lambda_t$ and $A_2 = 0.04 \pm 0.02$ for $\lambda_{\text{tot}} > \lambda_t$. In the right panel Figure 2, the blue dashed line represents the linear fit of the data. The vertical line represents the transition Eddington ratio (λ_t). The dark green and black lines represent the best-fit line for $\lambda_{\text{tot}} < \lambda_t$ and $\lambda_{\text{tot}} > \lambda_t$, respectively.

We repeated the above exercise for L_{Compt} and Γ . The Γ was observed to be anti-correlated with the L_{Compt} with the Pearson correlation coefficient $r = -0.599$ with the p-value of $< 10^{-4}$ in the HCS. Linear regression analysis returned as $\Gamma = (-0.12 \pm 0.006) + (6.00 \pm 0.23)$. Similar to the $\Gamma - L_{\text{tot}}$ correlation, two different correlation branches were observed in $\Gamma - L_{\text{Compt}}$ relation. The turnover was observed at $L_{t,\text{Compt}} \simeq 10^{37.15}$, i.e., $L_{t,\text{Compt}} \simeq 1.4 \times 10^{37} \text{ erg s}^{-1}$. The linear slope was obtained as -0.15 ± 0.01 for $L_{\text{Compt}} < L_{t,\text{Compt}}$ and 0.003 ± 0.021 for $L_{\text{Compt}} > L_{t,\text{Compt}}$.

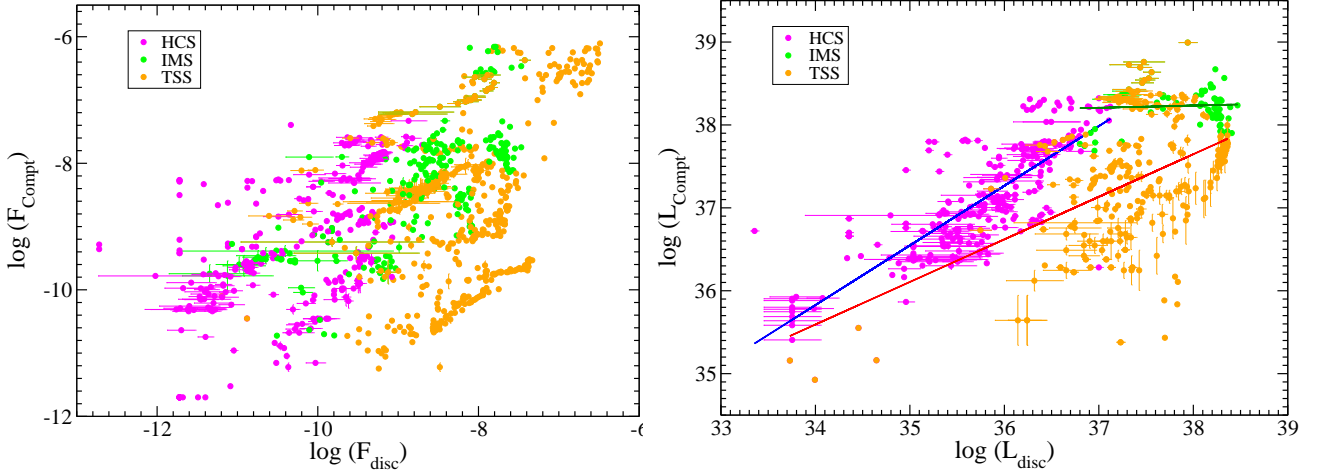


Figure 1. Left panel: the Comptonized flux (F_{Compt}) plotted as a function the disc flux (F_{disc}). Right panel: the Comptonized luminosity (L_{Compt}) is plotted as a function of the disc luminosity (L_{disc}). The magenta, green and orange points represent the observations from the HCS, IMS and TSS, respectively. The blue, dark green and red solid lines represent the linear best fit for the HCS, IMS and TSS, respectively, in the right panel.

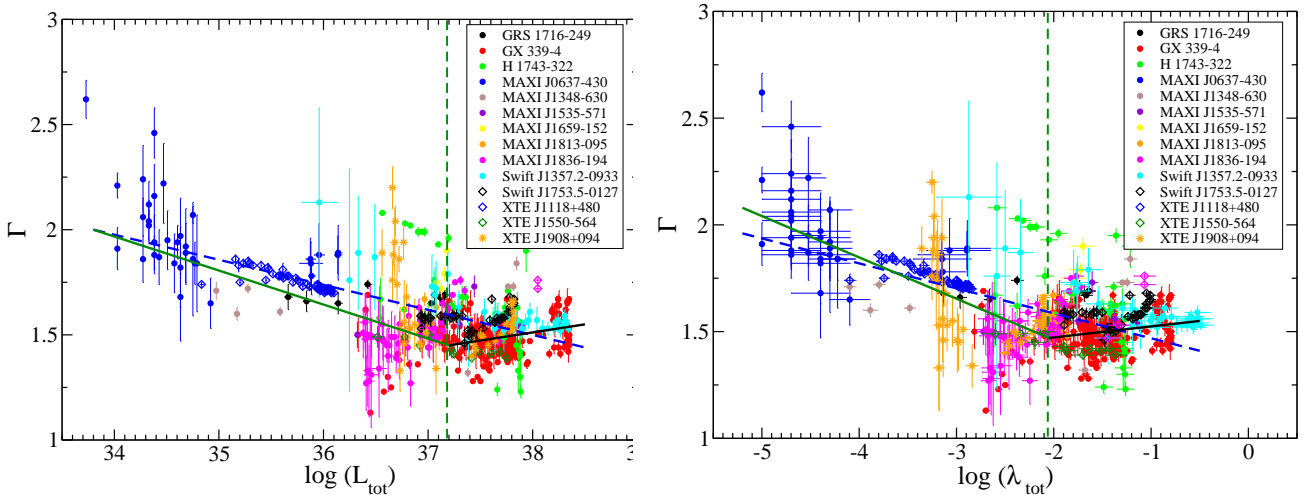


Figure 2. Left panel: the photon index (Γ) is plotted as a function of the total luminosity (L_{tot}) in the HCS. The blue dashed line represents the linear best fit. The dark green and black lines represents the best-fit line for $L_{\text{tot}} < L_t$ and $L_{\text{tot}} > L_t$, respectively. The dark green vertical line represents the transition luminosity (L_t). The sources with known distances are only considered in this plot. Right panel: the variation of the photon index (Γ) is shown as a function of the total Eddington ratio (λ_{tot}) for the HCS. The blue dashed line represents the linear best fit. The dark green and black lines represent the best-fit line for $\lambda_{\text{tot}} < \lambda_t$ and $\lambda_{\text{tot}} > \lambda_t$, respectively. The dark green vertical line represents the transition Eddington ratio (λ_t). Different colours and symbols correspond to the different sources mentioned in the inset of each figure. The sources with known masses and distances are considered in this plot.

No correlation between Γ and L_{Compt} was found in the IMS and TSS.

3.3 Hot Electron's Temperature

The information of kT_e or E_{cut} were available for four BHXBs in our sample. Figure 3 shows the variation of the Γ with the kT_e in the left panel. The Pearson correlation coefficient between Γ and kT_e is found to be 0.25 with the p-value $< 10^{-4}$, indicating no correlation. A linear fitting gives $\Gamma = (0.001 \pm 0.003)kT_e + (1.49 \pm 0.16)$. It seems that two different correlations exist for the high and low-temperature regions. We performed similar linear regression analysis as in §3.2, to check the different correlations of Γ and kT_e in

two different regions of kT_e . We obtained the slope of linear relation as $A_1 = 0.002 \pm 0.001$ for $kT_e < 30$ keV and $A_2 = -0.002 \pm 0.006$ for $kT_e > 30$ keV, respectively. The turn-over of correlation in $\Gamma - kT_e$ relation was not statistically significant. In the left panel of Figure 3, the blue dashed, solid black and solid red lines represent the linear best-fit for the entire data, for $kT_e < 30$ keV and for $kT_e > 30$ keV, respectively.

In the right panel of Figure 3, we plot kT_e as a function of the L_{Compt} . We did not find any correlation between kT_e and L_{Compt} in our sample. The Pearson correlation coefficient was $r = 0.25$ with a p-value of 0.403. A linear regression analysis returned with $\log L_{\text{Compt}} = (-1.61 \pm 0.32)kT_e + (99.2 \pm 19)$, indicating a negative corre-

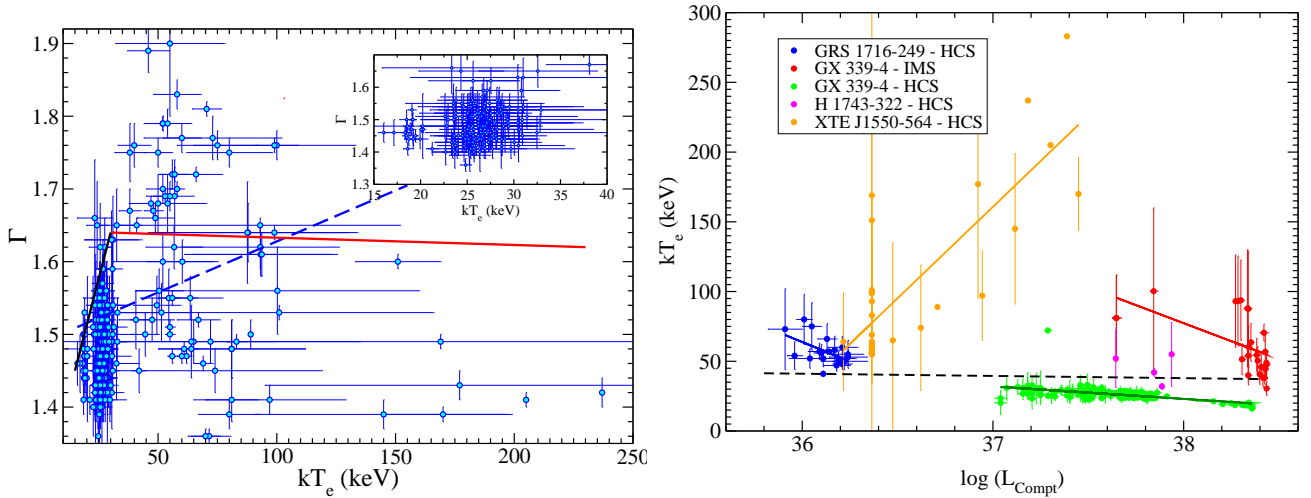


Figure 3. Left panel: variation of the photon index (Γ) is plotted as a function of the hot electrons temperature (kT_e). The blue dashed, solid black and solid red lines represent the linear best-fit for the entire data, for $kT_e < 30$ keV and for $kT_e > 30$ keV, respectively. The inset figure show the zoomed-in for clarity. Right panel: the variation hot electrons temperature (kT_e) is shown as a function of the Comptonized luminosity (L_{Compt}). The black dashed, solid blue, solid red, solid dark green, solid magenta and solid orange line represent the best linear fit for the entire sample, GRS 1716–249 in the HCS, GX 339–4 in the HCS, GX 339–4 in the IMS, and XTE J155–564 in the HCS, respectively. The blue, red, green, magenta and orange circles represent the data points for GRS 1716–249 in the HCS, GX 339–4 in the HCS, GX 339–4 in the IMS, H 1743–322 in the HCS, and XTE J155–564 in the HCS, respectively.

lation. For individual sources, the negative correlation was stronger than the entire sample. In the right panel of Figure 3, the blue, green, red, magenta and orange circles represent the data of GSR 1716–249 in the HCS, GX 339–4 in the HCS, GX 339–4 during the state transition/IMS, H1743–322 in the HCS and XTE J1550–564 in the HCS, respectively. Except for XTE J1550–564, a negative correlation between the kT_e and L_{Compt} was observed for the rest of the sources. We obtained the Pearson correlation coefficient $r = -0.53$ with the p-value of 0.01 for GRS 1716–249, -0.540 with p-value of 0.004 for GX 339–4 in the IMS, -0.587 with the p-value of < 0.001 for GX 339–4 in the HCS, 0.797 with the p-value of < 0.001 for XTE J1550–564, respectively. We did not calculate the correlation coefficient for H1743–322 as fewer than 11 data points were available. A linear regression analysis returned with different slopes for different sources, with -56.1 ± 21.0 for GRS 1716–249 in the HCS, 51.7 ± 16.4 GX 339–4-in the IMS, -9.0 ± 0.9 for GX 339–4 in the HCS, and 131.2 ± 19.5 for XTE J1550+564 in the HCS. As different source show different correlations, no correlation between the kT_e and L_{Compt} is seen. We also studied the correlation of kT_e with the λ_{Compt} . We obtained a similar correlation of kT_e with λ_{Compt} as L_{Compt} .

3.4 Disc Temperature

The disc flux is expected to vary with the T_{in} as $F_{\text{disc}} \propto T_{\text{in}}^4$. This relation holds if the R_{in} and the colour correction factor (κ) remain constant. We expect this relation to hold in the TSS as the disc extends to the innermost stable circular orbit (ISCO). Figure 4 shows the variation of the F_{disc} as a function of the T_{in} for nine sources in the TSS. In each panel, the solid red line represents the best fit by the linear regression method. The fit was done using the relation, $\log(F_{\text{disc}}) = A * \log(T_{\text{in}}) + B$. The details result of the linear fit is presented in Table 2.

Table 2. $F_{\text{disc}} - T_{\text{in}}$ Relation

Source	A	B
GX 339–4	4.27 ± 0.85	-7.48 ± 0.18
H 1743–322	3.78 ± 0.12	-7.81 ± 0.13
MAXI J0637–430	4.00 ± 0.10	-7.20 ± 0.14
MAXI J1727–203	4.03 ± 0.10	-6.29 ± 0.16
XTE J1550–564	3.54 ± 0.10	-7.28 ± 0.31
XTE J1652–223	4.29 ± 0.29	-7.07 ± 0.15
XTE J1748–288	6.14 ± 0.94	-8.71 ± 0.32
XTE J1817–330	6.07 ± 0.10	-7.42 ± 0.14
XTE J1908+094	5.31 ± 0.89	-7.94 ± 0.19

The result of the linear regression of the L_{disc} and T_{in} . The data are fitted with $\log(F_{\text{disc}}) = A * \log(T_{\text{in}}) + B$ in the TSS.

Out of a total of 20 sources, nine sources show TSS during their respective outbursts. Of these nine sources, $F_{\text{disc}} \propto T_{\text{in}}^4$ hold for the six sources in the TSS. Three sources, namely, XTE J1748–288, XTE J1817–330 and XTE J1908+094 showed deviation from the standard $F_{\text{disc}} \propto T_{\text{in}}^4$ relation.

3.5 Inner disc Radius

The R_{in} can be obtained from the DISKBB normalization (see Section 2.3), assuming a Schwarzschild black hole. During an outburst, an evolving disc is often observed with the disc moving in or out. Here we studied the variation of the R_{in} with the F_{disc} . In our sample, the information of the R_{in} was available for 14 sources. We show the variation of R_{in} with the F_{disc} in Figure 5. The horizontal black dashed line represents $R_{\text{in}} = 1.24 R_G$, which is the location of ISCO for a maximally rotating BH. Many points lie below the $R_{\text{in}} = 1.24 R_G$ line, which is unphysical. For $R_{\text{in}} > 1.24 R_G$, we did not observe any clear patterns of the variation of

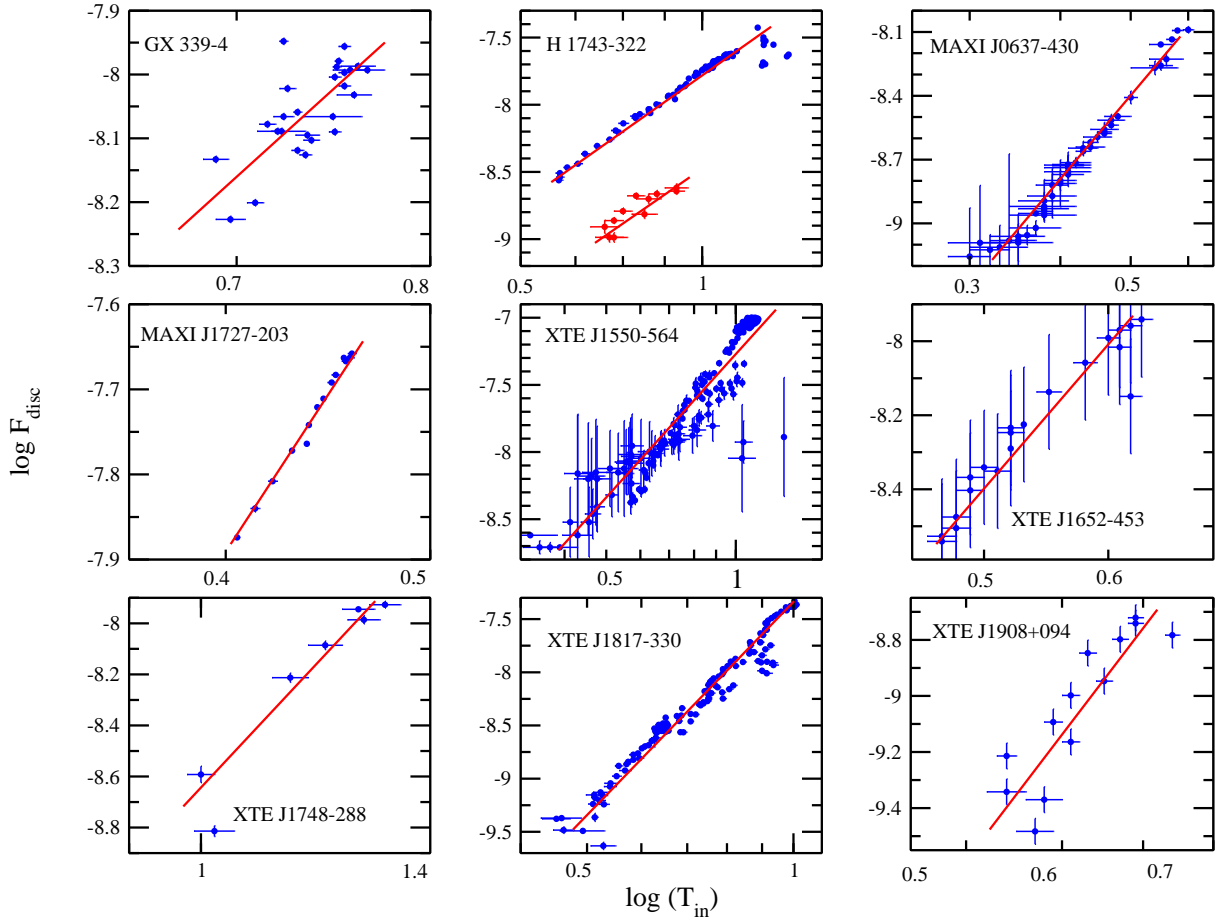


Figure 4. The disc flux (F_{disc}) is plotted as a function of the inner disc temperature (T_{in}) for nine BHXBs. Solid red lines represent the best-fit by linear regression using $\log F_{\text{disc}} = A * \log T_{\text{in}} + B$.

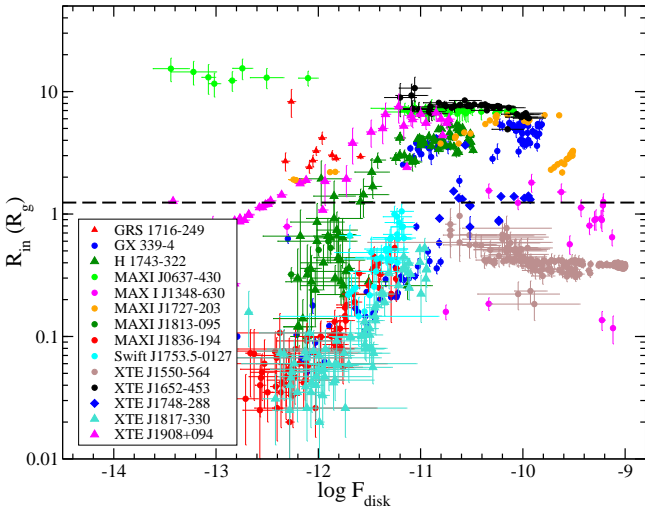


Figure 5. Inner disc radius (R_{in}) plotted as a function of the disc flux (F_{disc}). Different points represent different sources.

R_{in} with F_{disc} . Although some sources, e.g., MAXI J0637–430, XTE J1652–253, showed a negative correlation while others, e.g., MAXI J1727–203, XTE J1908+094, indicated a positive correlation.

3.6 Iron Line & Reprocessed Emission

The left panel of Figure 6 shows the variation of the F_{line} as a function of the F_{disc} and F_{Compt} in the HCS, IMS and TSS. The black circles, red diamonds and green up-triangles denote the disc flux in the HCS, IMS and TSS, respectively. The Comptonized flux in the HCS, IMS and TSS are shown by blue circles, magenta squares and dark green down-triangles, respectively. The solid black, red and green lines represent the linear best-fit for F_{disc} in the HCS, IMS and TSS, respectively, while the solid blue, magenta and dark green lines represent the linear best-fit for the F_{Compt} in the HCS, IMS and TSS, respectively. In the right panel of Figure 6, We show the variation of $F_{\text{line}}/F_{\text{Compt}}$ as a function of the Γ . The blue, magenta and green circles represent the data points from the HCS, IMS and TSS, respectively. The black, red and green dashed lines represent the linear best fit for $\Gamma < 2.3$, $2.3 < \Gamma < 3.9$, and $\Gamma > 3.9$, respectively.

In our sample, the iron line was detected for 10 BHXBs. We found that the F_{line} is correlated with the F_{disc} and F_{Compt} for the whole sample with the Pearson correlation coefficient of 0.738 with the p-value of $< 10^{-4}$ and 0.897 with the p-value of $< 10^{-4}$, respectively. However, when we considered the data within individual spectral states, the correlation of F_{disc} and F_{line} breaks down slightly. The F_{disc} was found to be moderately correlated with the F_{line} ; with

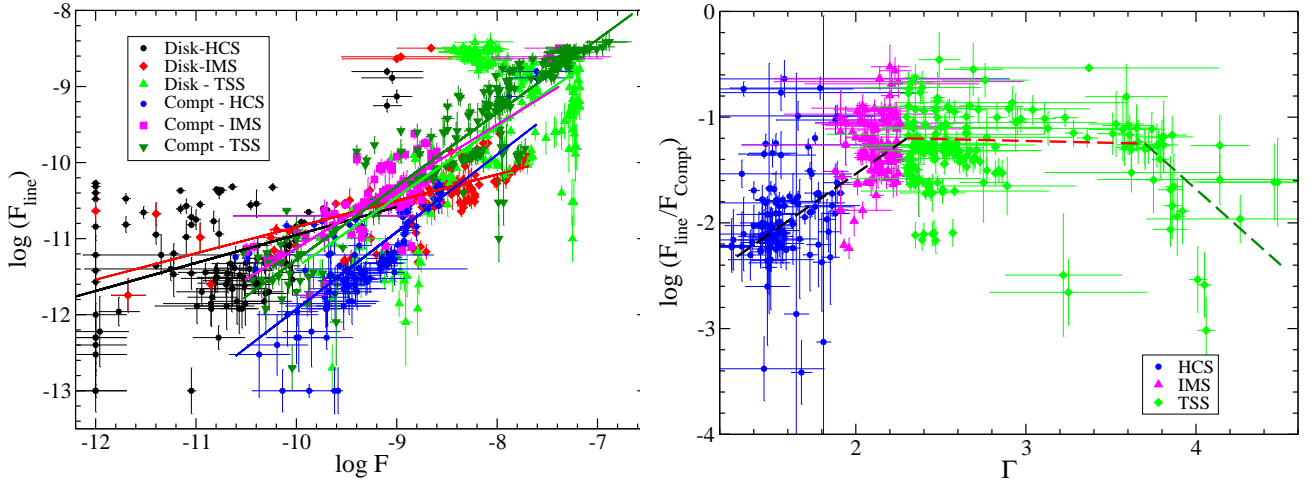


Figure 6. Left panel: variation of the line flux (F_{line}) is plotted as a function of disc (F_{disc}) and Comptonized flux (F_{Compt}) in the HCS, IMS and TSS. The black circles, red diamonds and green up-triangles represent the disc flux in the HCS, IMS and TSS, respectively. The Comptonized flux in the HCS, IMS and TSS are shown by blue circles, magenta squares and dark green down-triangles, respectively. The solid black, red and green lines represent the linear best-fit for F_{disc} in the HCS, IMS and TSS, respectively, while the solid blue, magenta and dark green lines represent the linear best-fit for the F_{Compt} in the HCS, IMS and TSS, respectively. Right panel: the variation of the ratio of the line flux to the Comptonized flux ($F_{\text{line}}/F_{\text{Compt}}$) is shown as a function of the photon index (Γ), in the HCS, IMS, and TSS, respectively. The blue circles, magenta triangles and green circles represent the data from the HCS, IMS and TSS, respectively. The black dashed, red dashed and dark green dashed lines represent the linear best fit for the region $\Gamma < 2.3$, $2.3 < \Gamma < 3.9$, and $\Gamma > 3.9$, respectively.

the Pearson correlation coefficient: $r = 0.418$ with the p-value of $< 10^{-4}$ in the HCS, $r = 0.554$ with the p-value of $< 10^{-4}$ in the IMS, and $r = 0.634$ with the p-value of $< 10^{-4}$ in the TSS. The F_{Compt} was observed to be strongly correlated with the F_{line} in all spectral states; with the Pearson correlation coefficient $r = 0.768$ with the p-value of $< 10^{-4}$ in the HCS, $r = 0.854$ with the p-value of $< 10^{-4}$ in the IMS, and $r = 0.926$ with the p-value of $< 10^{-4}$ in the TSS.

We also conducted linear regression analysis of F_{line} with the F_{disc} and F_{Compt} . A linear regression analysis yields the slope of 1.03 ± 0.05 and 0.71 ± 0.02 for F_{disc} and F_{Compt} , respectively, for the entire sample. Considering the individual spectral state, we obtained the slope as 0.37 ± 0.09 in the HCS, 0.35 ± 0.09 in the IMS and 0.92 ± 0.18 in the TSS for F_{disc} . For F_{Compt} , the slopes are obtained as 1.02 ± 0.07 in the HCS, 0.81 ± 0.05 in the IMS and 0.97 ± 0.03 in the TSS.

We found that the Γ is moderately correlated with the $F_{\text{line}}/F_{\text{Compt}}$ with $r = 0.346$ with the p-value of $< 10^{-4}$ in the HCS. No correlation was found between the Γ and $F_{\text{line}}/F_{\text{Compt}}$ in the IMS and TSS, respectively. When we performed linear regression analysis, we found the slope as 1.10 ± 0.08 for $\Gamma < 2.3$, -0.01 ± 0.05 for $2.3 < \Gamma < 3.9$ and 1.73 ± 0.91 for $\Gamma > 3.9$.

4 DISCUSSION AND CONCLUDING REMARKS

We collected spectral data from 32 outbursts of 20 BHXBs from the literature. We checked for correlations among different spectral parameters to understand the accretion evolution across different spectral states on a global scale.

A BHXB is generally observed in the HCS at the beginning of the outburst. As the accretion rate increases, the source evolves through various spectral states. Both

F_{disc} and F_{Compt} evolve during an outburst. Generally, at the start of the outburst, F_{disc} is low, increasing as the source evolves and becoming maximum in the TSS. The F_{disc} depends on the R_{in} and the T_{in} as $F_{\text{disc}} \propto R_{\text{in}}^2 T_{\text{in}}^4$ (e.g., Shakura & Sunyaev 1973; Dunn et al. 2011). In the TSS, the F_{disc} varies as $F_{\text{disc}} \propto T_{\text{in}}^4$, given that R_{in} and the colour correction factor (κ) remains constant (eg., Shimura & Takahara 1995). In our sample, the data for the TSS were available for nine sources, and out of these nine sources, six sources closely followed this relation. Moving disc or changing κ could be the reason for not following the theoretical relation for the rest three sources. In the IMS and HCS, no sources were found to follow this relation. This is expected as the disc may move in the IMS and HCS (e.g., Gierliński & Done 2004; Dunn et al. 2010, 2011).

The evolution of the R_{in} is still debated. It is generally accepted that the R_{in} extends to the ISCO in the TSS; however, it is unclear in the HCS and IMS. Our study did not observe any clear pattern of the variation of R_{in} with the F_{disc} . For some sources, e.g., MAXI J0637–430, XTE J1652–253, R_{in} was found to correlate negatively with the F_{disc} , i.e., the disc moved outward when the outburst started. For some other sources, e.g., MAXI J1727–203, XTE J1908+094, R_{in} was observed to positively correlate with the F_{disc} , i.e., the disc moved closer to the BH during the outburst. However, in our sample, the variation of the R_{in} is unclear for most sources. Hence, the current study could not confirm the evolution of the inner disc.

It is well known that the T_{in} and N_{dobb} are degenerate. In many observations, T_{in} was higher in the HCS with very small N_{dobb} . These are not physical. Most of the studies were done using *RXTE*/PCA, which had a limited band-pass at the lower end of the spectra, which might cause the inaccurate estimation of the T_{in} and N_{DDB} or R_{in} , particularly in the HCS. In general, the disc emits the maximum amount

of power at $\sim 3 kT_{\text{in}}$. The *Swift* /XRT or *NICER* extends up to ~ 0.5 keV while *RXTE*/PCA extends ~ 2 keV at the lower end of the spectra. PCA only detects a small part of the disc emission, much beyond the Wien peak in most cases (especially in the HCS), and thus, contrary to the XRT, is not appropriate to estimate the disc properties precisely. Additionally, DISKBB considers a non-rotating BH. Thus, non-relativistic model such as DISKBB may not calculate the R_{in} accurately. Hence, robust relativistic modelling in a broad energy band is required to study the evolution of the disc accurately.

A fraction of the seed photons intercepted with the corona and produced the hard Comptonized photons via inverse-Comptonization (e.g., Sunyaev & Titarchuk 1980, 1985; Zdziarski et al. 1996). The Comptonized spectra is generally characterized by the spectral slope or photon index (Γ). In the HCS and TSS, we observed that the L_{Compt} is strongly correlated with the L_{disc} . This suggested that as the disc luminosity or the number of the seed photons increase, more photons intercept at the corona, producing higher Comptonized emission.

The accretion geometry is observed to differ in the HCS from the TSS. The evidence comes from the different correlation of Γ and L_{tot} in the HCS and TSS (e.g., Wu & Gu 2008; Yang et al. 2015). When the accretion rate is high, the standard disc supplies the seed photons to the corona, resulting in efficient cooling. This leads to a drop in the hot electron temperature and softer spectra. Thus, the thermal Comptonization naturally explains the positive correlation of $\Gamma - L_{\text{tot}}$ and the negative correlation of $kT_e - L_{\text{tot}}$. However, when the accretion rate drops, the inner accretion disc is replaced by a hot accretion flow or radiatively inefficient flow (e.g., Yuan & Zdziarski 2004; Yuan & Narayan 2014). In this state, most of the seed photons are non-thermal and originate in the corona itself or jet (e.g., Markoff et al. 2001; Yang et al. 2015). This explains the negative correlation of $\Gamma - L_{\text{tot}}$ and positive correlation of $kT_e - L_{\text{tot}}$ (e.g., Yang et al. 2015; Yan et al. 2020).

We observed a negative correlation between the Γ and L_{Compt} for $L_{\text{Compt}} < 1.4 \times 10^{37}$ erg s $^{-1}$ while a positive correlation is observed for $L_{\text{Compt}} > 1.4 \times 10^{37}$ erg s $^{-1}$. In terms of the total luminosity, the turn-over occurs at $L_{\text{tot}} \approx 1.5 \times 10^{37}$ erg s $^{-1}$. Yan et al. (2020) found the turn-over at slightly lower luminosity at $L_{\text{tot}} \sim 9 \times 10^{36}$ erg s $^{-1}$. The turn-over of the correlation or ‘V’-shaped correlation of $\Gamma - L_{\text{tot}}$ indicates that the disc photons still play an important role in the HCS, if not a dominant one.

We did not observe any correlation of the Γ and kT_e in our sample. Along with the kT_e , the Γ of the emergence spectra also depends on the optical depth (τ) of the Compton cloud. The non-correlation between Γ and kT_e has been observed in other BHXBs (e.g., Miyakawa et al. 2008). Generally, it is expected that the high kT_e would result in hard spectra, i.e. Γ would anti-correlated with the kT_e , only if τ remains constant.

We also did not find any correlation between the kT_e and L_{Compt} in our sample. This is largely because one source behaves differently. Actually, different correlations are found for each source. A negative correlation between the kT_e and L_{Compt} was observed for GX 339–4, GRS 1716–249 and H 1743–322, while a positive correlation was observed for XTE J1550–564. Both negative and positive correla-

tion of kT_e and L_{Compt} has been observed in BHXBs (e.g., Zdziarski et al. 2004; Yamaoka et al. 2005).

We observed that the F_{line} is correlated with both the F_{disc} and the F_{Compt} , indicating the reprocessed emission depend on both disc and coronal emission. The correlation of the F_{line} is stronger in the TSS, implying that the reprocessing is stronger if the disc is prominent. We also found that the ratio of the line flux to the Comptonized flux ($F_{\text{line}}/F_{\text{Compt}}$) is positively correlated with the Γ for the region $\Gamma < 2.3$, no correlation for $3.8 < \Gamma < 2.3$, and negatively correlation for $\Gamma > 3.8$. This result implies that the strength of the reprocessed emission increases as the source moves toward the TSS from the HCS, with the increasing disc flux. However, after a certain point, the Comptonized flux decreases, and the reflection drops due to the lack of hard photons. Similar correlation of the Γ and reflection fraction has been observed for both BHXBs (e.g., Zdziarski et al. 1999) and active galactic nuclei (e.g., Ezhikode et al. 2020).

The IMS is complex in comparison to the HCS and TSS. The IMS is considered to be the state transition phase between the HCS and TSS. The accretion geometry is distinct in the HCS and TSS and is believed to change during the IMS. We observed a correlation between L_{disc} and L_{Compt} in the HCS and TSS, but no correlation is observed in the IMS. The IMS is associated with the flaring events (e.g., Fender & Belloni 2004; Remillard & McClintock 2006), which makes the IMS complex. A part of the X-ray emission could come from the flare (e.g., Jana et al. 2017), resulting in non-correlations among the spectral parameters. In general, we did not observe any clear pattern of the spectral parameters in the IMS in our study. Historically, the HCS and TSS are studied in detail, whereas the IMS has not been studied extensively. However, recently, some black holes are studied in the state transition phase (e.g., Jana et al. 2022; Kong et al. 2021; Cúneo et al. 2020).

BHXBs show rich phenomenology in both spectral and timing properties. Here, we collected the data from the literature to understand phenomenology on a global scale. The black hole accretion is studied for over half a decade now. We now understand reasonably well how the accretion process works around a black hole. However, we still lack some knowledge of the black hole accretion, especially during the state transition. Additionally, the evolution of the accretion disc in the HCS is still debated. The study of BHXBs with Phenomenological models gave us a good understanding of the accretion process; however, it is far from the complete picture. To understand the BHXB completely, one needs to study the BHXB with a more physical model that considers the relativistic effect. In this work, we discuss how spectral properties of BHXB from a phenomenological perspective. Furthermore, the timing properties of BHXB from the phenomenological perspective will be studied in future.

ACKNOWLEDGEMENTS

We thank the anonymous reviewer for constructive suggestion and comments that improved the manuscript significantly. We would also like to thank Arka Chatterjee, Claudio Ricci, Debjit Chatterjee, Dipak Debnath, Gaurava K.

Jaisawal, Hsiang-Kuang Chang, Prantik Nandi, Sachindra Naik, Sandip K. Chakrabarti and Santanu Mondal for helping me to understand the subject over the year.

DATA AVAILABILITY

We have taken the data from the literature. Appropriate references are included in the text.

REFERENCES

- Alabarta K., et al., 2020, *MNRAS*, **497**, 3896
- Armas Padilla M., Degenaar N., Russell D. M., Wijnands R., 2013, *MNRAS*, **428**, 3083
- Armas Padilla M., Wijnands R., Altamirano D., Méndez M., Miller J. M., Degenaar N., 2014, *MNRAS*, **439**, 3908
- Armas Padilla M., Muñoz-Darias T., Sánchez-Sierras J., De Marco B., Jiménez-Ibarra F., Casares J., Corral-Santana J. M., Torres M. A. P., 2019, *MNRAS*, **485**, 5235
- Bassi T., et al., 2019, *MNRAS*, **482**, 1587
- Belloni T., Homan J., Casella P., van der Klis M., Nespoli E., Lewin W. H. G., Miller J. M., Méndez M., 2005, *A&A*, **440**, 207
- Cadolle Bel M., et al., 2007, *ApJ*, **659**, 549
- Capitanio F., Belloni T., Del Santo M., Ubertini P., 2009, *MNRAS*, **398**, 1194
- Casella P., Belloni T., Stella L., 2005, *ApJ*, **629**, 403
- Chakrabarti S., Titarchuk L. G., 1995, *ApJ*, **455**, 623
- Chatterjee D., Debnath D., Jana A., Chakrabarti S. K., 2019, *Ap&SS*, **364**, 14
- Chatterjee D., Jana A., Chatterjee K., Bhowmick R., Nath S. K., Chakrabarti S. K., Mangalam A., Debnath D., 2021a, *Galaxies*, **9**, 25
- Chatterjee K., Debnath D., Chatterjee D., Jana A., Nath S. K., Bhowmick R., Chakrabarti S. K., 2021b, *Ap&SS*, **366**, 63
- Chauhan J., et al., 2019, *MNRAS*, **488**, L129
- Chauhan J., et al., 2021, *MNRAS*, **501**, L60
- Chen Y. P., Zhang S., Torres D. F., Wang J. M., Li J., Li T. P., Qu J. L., 2010, *A&A*, **522**, A99
- Cúneo V. A., et al., 2020, *MNRAS*, **496**, 1001
- Curran P. A., et al., 2015, *MNRAS*, **451**, 3975
- Debnath D., Molla A. A., Chakrabarti S. K., Mondal S., 2015, *ApJ*, **803**, 59
- Debnath D., Jana A., Chakrabarti S. K., Chatterjee D., Mondal S., 2017, *ApJ*, **850**, 92
- Debnath D., Chatterjee D., Jana A., Chakrabarti S. K., Chatterjee K., 2020, *Research in Astronomy and Astrophysics*, **20**, 175
- Della Valle M., Mirabel I. F., Rodriguez L. F., 1994, *A&A*, **290**, 803
- Dinçer T., Kalemci E., Buxton M. M., Bailyn C. D., Tomsick J. A., Corbel S., 2012, *ApJ*, **753**, 55
- Done C., Gierliński M., Kubota A., 2007, *A&ARv*, **15**, 1
- Draghis P. A., Miller J. M., Zoghbi A., Kammoun E. S., Reynolds M. T., Tomsick J. A., 2021, *ApJ*, **920**, 88
- Dunn R. J. H., Fender R. P., Kōrding E. G., Belloni T., Cabanac C., 2010, *MNRAS*, **403**, 61
- Dunn R. J. H., Fender R. P., Kōrding E. G., Belloni T., Merloni A., 2011, *MNRAS*, **411**, 337
- Ezhikode S. H., Dewangan G. C., Misra R., Philip N. S., 2020, *MNRAS*, **495**, 3373
- Fabian A. C., Rees M. J., Stella L., White N. E., 1989, *MNRAS*, **238**, 729
- Fender R., Belloni T., 2004, *ARA&A*, **42**, 317
- Gierliński M., Done C., 2004, *MNRAS*, **347**, 885
- Gierliński M., Done C., Page K., 2008, *MNRAS*, **388**, 753
- Göğüş E., et al., 2004, *ApJ*, **609**, 977
- Haardt F., Maraschi L., 1993, *ApJ*, **413**, 507
- Han P., Qu J., Zhang S., Wang J., Song L., Ding G., Yan S., Lu Y., 2011, *MNRAS*, **413**, 1072
- Homan J., Belloni T., 2005, *Ap&SS*, **300**, 107
- Homan J., Wijnands R., van der Klis M., Belloni T., van Paradijs J., Klein-Wolt M., Fender R., Méndez M., 2001, *ApJS*, **132**, 377
- Ingram A. R., Motta S. E., 2019, *New Astron. Rev.*, **85**, 101524
- Jana A., Debnath D., Chakrabarti S. K., Mondal S., Molla A. A., 2016, *ApJ*, **819**, 107
- Jana A., Chakrabarti S. K., Debnath D., 2017, *ApJ*, **850**, 91
- Jana A., Debnath D., Chakrabarti S. K., Chatterjee D., 2020, *Research in Astronomy and Astrophysics*, **20**, 028
- Jana A., Jaisawal G. K., Naik S., Kumari N., Chhotaray B., Altamirano D., Remillard R. A., Gendreau K. C., 2021a, *MNRAS*, **504**, 4793
- Jana A., et al., 2021b, *Research in Astronomy and Astrophysics*, in Press.
- Jana A., Naik S., Jaisawal G. K., Chhotaray B., Kumari N., Gupta S., 2022, *MNRAS*, **511**, 3922
- Jia N., et al., 2022, *MNRAS*, **511**, 3125
- Kalemci E., Tomsick J. A., Rothschild R. E., Pottschmidt K., Corbel S., Kaaret P., 2006, *ApJ*, **639**, 340
- Khargharia J., Froning C. S., Robinson E. L., Gelino D. M., 2013, *AJ*, **145**, 21
- Kong L. D., et al., 2021, *ApJ*, **906**, L2
- Kreidberg L., Bailyn C. D., Farr W. M., Kalogera V., 2012, *ApJ*, **757**, 36
- Kubota A., Tanaka Y., Makishima K., Ueda Y., Dotani T., Inoue H., Yamaoka K., 1998, *PASJ*, **50**, 667
- Kuulkers E., et al., 2013, *A&A*, **552**, A32
- Lazar H., et al., 2021, *ApJ*, **921**, 155
- Maccarone T. J., 2003, *A&A*, **409**, 697
- Makishima K., Maejima Y., Mitsuda K., Bradt H. V., Remillard R. A., Tuohy I. R., Hoshi R., Nakagawa M., 1986, *ApJ*, **308**, 635
- Markoff S., Falcke H., Fender R., 2001, *A&A*, **372**, L25
- Matt G., Perola G. C., Piro L., 1991, *A&A*, **247**, 25
- McClintock J. E., Garcia M. R., Caldwell N., Falco E. E., Garnavich P. M., Zhao P., 2001, *ApJ*, **551**, L147
- McClintock J. E., Remillard R. A., Rupen M. P., Torres M. A. P., Steeghs D., Levine A. M., Orosz J. A., 2009, *ApJ*, **698**, 1398
- Méndez M., van der Klis M., 1997, *ApJ*, **479**, 926
- Mitsuda K., et al., 1984, *PASJ*, **36**, 741
- Miyakawa T., Yamaoka K., Homan J., Saito K., Dotani T., Yoshida A., Inoue H., 2008, *PASJ*, **60**, 637
- Molla A. A., Debnath D., Chakrabarti S. K., Mondal S., Jana A., 2016, *MNRAS*, **460**, 3163
- Molla A. A., Chakrabarti S. K., Debnath D., Mondal S., 2017, *ApJ*, **834**, 88
- Mondal S., Chakrabarti S. K., 2019, *MNRAS*, **483**, 1178
- Mondal S., Debnath D., Chakrabarti S. K., 2014, *ApJ*, **786**, 4
- Muñoz-Darias T., Motta S., Belloni T. M., 2011, *MNRAS*, **410**, 679
- Nandi A., Chakrabarti S. K., Vadawale S. V., Rao A. R., 2001, *A&A*, **380**, 245
- Nandi A., Debnath D., Mandal S., Chakrabarti S. K., 2012, *A&A*, **542**, A56
- Neustroev V. V., Veledina A., Poutanen J., Zharikov S. V., Tsygankov S. S., Sjöberg G., Kajava J. J. E., 2014, *MNRAS*, **445**, 2424
- Orosz J. A., et al., 2002, *ApJ*, **568**, 845
- Orosz J. A., Steiner J. F., McClintock J. E., Torres M. A. P., Remillard R. A., Bailyn C. D., Miller J. M., 2011, *ApJ*, **730**, 75
- Parker M. L., et al., 2016, *ApJ*, **821**, L6
- Petrucci P. O., et al., 2001, *ApJ*, **556**, 716

- Remillard R. A., McClintock J. E., 2006, *ARA&A*, **44**, 49
- Revnivtsev M. G., Trudolyubov S. P., Borozdin K. N., 2000, *MNRAS*, **312**, 151
- Rodriguez J., Corbel S., Tomsick J. A., 2003, *ApJ*, **595**, 1032
- Russell T. D., Soria R., Motch C., Pakull M. W., Torres M. A. P., Curran P. A., Jonker P. G., Miller-Jones J. C. A., 2014a, *MNRAS*, **439**, 1381
- Russell T. D., Soria R., Miller-Jones J. C. A., Curran P. A., Markoff S., Russell D. M., Sivakoff G. R., 2014b, *MNRAS*, **439**, 1390
- Rykoff E. S., Miller J. M., Steeghs D., Torres M. A. P., 2007, *ApJ*, **666**, 1129
- Shakura N. I., Sunyaev R. A., 1973, *A&A*, **500**, 33
- Shang J. R., Debnath D., Chatterjee D., Jana A., Chakrabarti S. K., Chang H. K., Yap Y. X., Chiu C. L., 2019, *ApJ*, **875**, 4
- Shaw A. W., et al., 2016, *MNRAS*, **458**, 1636
- Shimura T., Takahara F., 1995, *ApJ*, **445**, 780
- Shui Q. C., et al., 2021, *MNRAS*, **508**, 287
- Sobczak G. J., McClintock J. E., Remillard R. A., Cui W., Levine A. M., Morgan E. H., Orosz J. A., Bailyn C. D., 2000, *ApJ*, **544**, 993
- Sreehari H., Iyer N., Radhika D., Nandi A., Mandal S., 2019, *Advances in Space Research*, **63**, 1374
- Steiner J. F., McClintock J. E., Reid M. J., 2012, *ApJ*, **745**, L7
- Stiele H., Kong A. K. H., 2018, *ApJ*, **852**, 34
- Sunyaev R. A., Titarchuk L. G., 1980, *A&A*, **500**, 167
- Sunyaev R. A., Titarchuk L. G., 1985, *A&A*, **143**, 374
- Tao L., et al., 2018, *MNRAS*, **480**, 4443
- Tao L., Tomsick J. A., Qu J., Zhang S., Zhang S., Bu Q., 2019, *ApJ*, **887**, 184
- Tetarenko B. E., Sivakoff G. R., Heinke C. O., Gladstone J. C., 2016, *ApJS*, **222**, 15
- Titarchuk L., 1994, *ApJ*, **434**, 570
- Torres M. A. P., Jonker P. G., Casares J., Miller-Jones J. C. A., Steeghs D., 2021, *MNRAS*, **501**, 2174
- Vahdat Motlagh A., Kalemci E., Maccarone T. J., 2019, *MNRAS*, **485**, 2744
- Van der Klis M., 1989, *ARA&A*, **27**, 517
- Van der Klis M., 1994, *ApJS*, **92**, 511
- Vasiliev L., Trudolyubov S., Revnivtsev M., 2000, *A&A*, **362**, L53
- Wu Q., Gu M., 2008, *ApJ*, **682**, 212
- Xu Y., et al., 2018, *ApJ*, **852**, L34
- Yamaoka K., Uzawa M., Arai M., Yamazaki T., Yoshida A., 2005, *Chinese Journal of Astronomy and Astrophysics Supplement*, **5**, 273
- Yan Z., Xie F.-G., Zhang W., 2020, *ApJ*, **889**, L18
- Yang Q.-X., Xie F.-G., Yuan F., Zdziarski A. A., Gierliński M., Ho L. C., Yu Z., 2015, *MNRAS*, **447**, 1692
- Yuan F., Narayan R., 2014, *ARA&A*, **52**, 529
- Yuan F., Zdziarski A. A., 2004, *MNRAS*, **354**, 953
- Zdziarski A. A., Johnson W. N., Magdziarz P., 1996, *MNRAS*, **283**, 193
- Zdziarski A. A., Lubiński P., Smith D. A., 1999, *MNRAS*, **303**, L11
- Zdziarski A. A., Gierliński M., Mikołajewska J., Wardziński G., Smith D. M., Harmon B. A., Kitamoto S., 2004, *MNRAS*, **351**, 791
- Zhao H. H., Weng S. S., Qu J. L., Cai J. P., Yuan Q. R., 2016, *A&A*, **593**, A23
- Zhou J. N., Liu Q. Z., Chen Y. P., Li J., Qu J. L., Zhang S., Gao H. Q., Zhang Z., 2013, *MNRAS*, **431**, 2285

This paper has been typeset from a $\text{\TeX}/\text{\LaTeX}$ file prepared by the author.